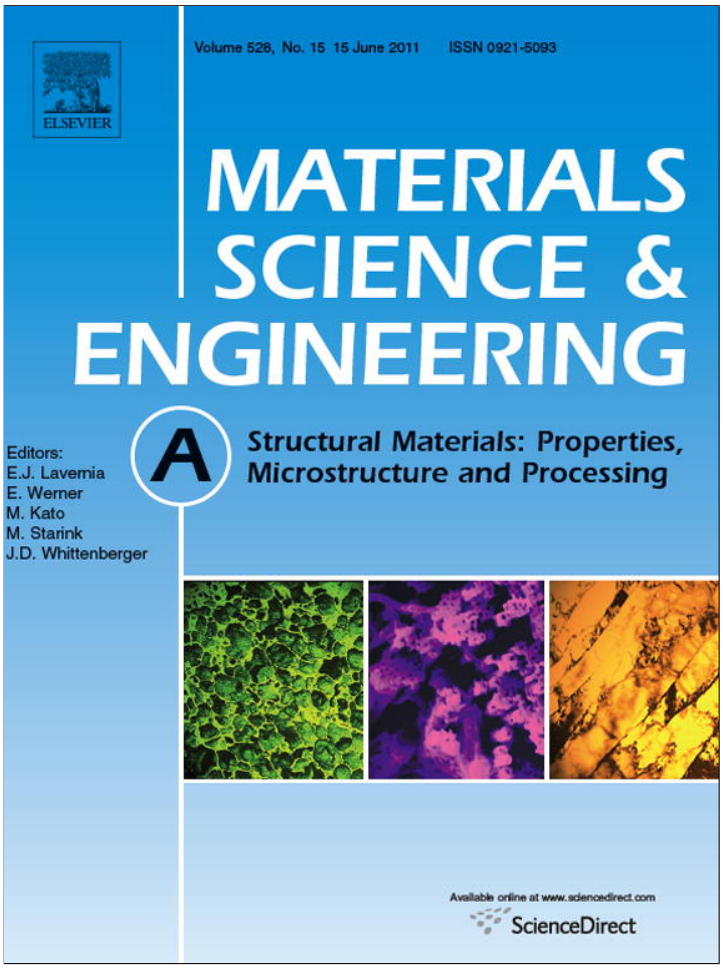

Materials Science and Engineering A 528 (2011) 4888–4898

Contents lists available at ScienceDirect

Materials Science and Engineering A

journal homepage: www.elsevier.com/locate/msea

A comparison of the microstructure and creep behavior of cold rolled HAYNES® 230 alloy™ and HAYNES® 282 alloy™

C.J. Boehlert*, S.C. Longanbach

Department of Chemical Engineering and Materials Science, Michigan State University, East Lansing, MI 48824, USA

ARTICLE INFO

Article history:
Received 20 September 2010
Received in revised form 10 January 2011
Accepted 3 March 2011
Available online 10 March 2011

Keywords:
Superalloy
Electron backscattered diffraction
Creep
Microstructure

ABSTRACT

HAYNES 282 and HAYNES 230 nickel-based superalloys were subjected to cold rolling deformation and heat treatments in order to investigate processing–microstructure–property relationships to understand the effects of thermomechanical processing on their microstructure and tensile-creep behavior. The sheet materials underwent four cycles of 20% reduction in thickness followed by a solution treatment. The resultant microstructures were characterized using electron backscattered diffraction and electron microscopy, and the high-temperature (973–1088 K (700–815 °C)) creep and fatigue behavior was evaluated and compared to the commercially available sheet alloys. The thermomechanical processing treatments did not significantly affect the grain boundary character distribution and almost half of all the boundaries in the microstructures were twin boundaries. The creep resistance was shown to degrade with the additional thermomechanical treatments, which resulted in finer equiaxed grain sizes. The HAYNES 282 alloy was shown to be significantly more creep resistant than the HAYNES 230 alloy. The fatigue behavior indicated that creep ratcheting occurred more prominently in the HAYNES 230 alloy than in the HAYNES 282 alloy and this was explained to be a result of the superior creep resistance exhibited by the HAYNES 282 alloy. Overall, this study suggests that additional energy-intensive processing treatments, beyond those involved in the commercially available sheet products, may not be beneficial for additional creep resistance.

1. Introduction

HAYNES 282 alloy is an advanced wrought γ′-strengthened nickel-based superalloy which is solid solution strengthened by cobalt (Co), chromium (Cr), and molybdenum (Mo). It was designed for improved high-temperature creep resistance, and its creep resistance surpasses that for Waspaloy and approaches that for R-41 alloy [1]. HAYNES 282 alloy possesses a unique combination of creep strength, thermal stability, weldability, and fabricability, and it is being considered for the transition sections and other hot-gas-path components in land-based gas turbines and for critical aircraft gas turbine applications, such as sheet fabrications, seamless and flash butt-welded rings, exhaust and nozzle components, and cases found in compressor, combustor, and turbine sections. It is easily deformed at room-temperature (RT) in its solution-treated condition, and it requires an aging treatment to obtain its exceptional high-temperature strength and creep resistance.

HAYNES 230 alloy, which contains Cr and tungsten (W) as its primary alloying elements, is another recently developed high-temperature, high-oxidation resistant, high-strength alloy. It can be worked, usually forged, in the temperature range between 1198 and 1448 K (925 and 1175 °C) [2], and it is projected for applications including gas turbine hot section components, such as combustion cans, thermocouple protection tubes, heat exchangers and industrial furnace fixtures and muffles. Unlike that for HAYNES 282 alloy, the solid solution strengthened HAYNES 230 alloy does not require an age-hardening heat treatment. HAYNES 230 alloy was designed for applications at higher temperatures where the γ′-strengthened alloys, such as HAYNES 282 alloy, lose strength due to γ′ solutionizing.

Each of these two alloys exhibits good fabricability, RT ductility, and an attractive balance of high-temperature tensile properties and oxidation resistance. However, HAYNES 282 alloy was designed for improved creep resistance in the temperature range of 922–1200 K (649–927 °C), which encompasses the target temperature range for this study (973–1088 K (700–815 °C)). HAYNES 230 alloy was designed for higher temperatures as mentioned above.

The current work was an attempt to identify and compare the processing–microstructure–property relationships in each alloy. As the mechanical deformation, creep behavior, and corrosion resistance of other superalloy systems have been

* Corresponding author at: Department of Chemical Engineering and Materials Science, Michigan State University, 2527 Engineering Building, East Lansing, MI 48824, USA. Tel.: +1 517 353 3703.
E-mail address: Boehlert@egr.msu.edu (C.J. Boehlert).

0921-5093/$ – see front matter © 2011 Elsevier B.V. All rights reserved.
doi:10.1016/j.msea.2011.03.019

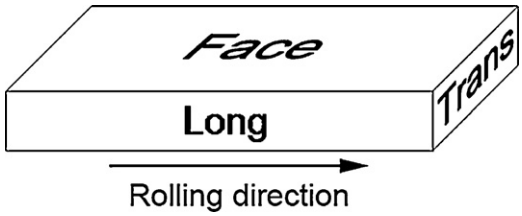

Fig. 1. A schematic illustrating the orientations of the rolled sheet materials.

improved through grain boundary character alteration using strain–recrystallization thermomechanical processing (TMP) treatments [3–19], the thought at the beginning of this work was there is the potential to improve the creep performance of HAYNES 230 and 282 alloys using a similar grain boundary engineering strategies. However, the TMP treatments used in this work resulted in decreased creep resistance, and a significant difference in the grain boundary character distribution (GBCP) between the baseline and TMP materials was not observed. The reasons for this behavior will be discussed and the results will be compared to that for a cobalt-based Udimet 188 alloy [20].

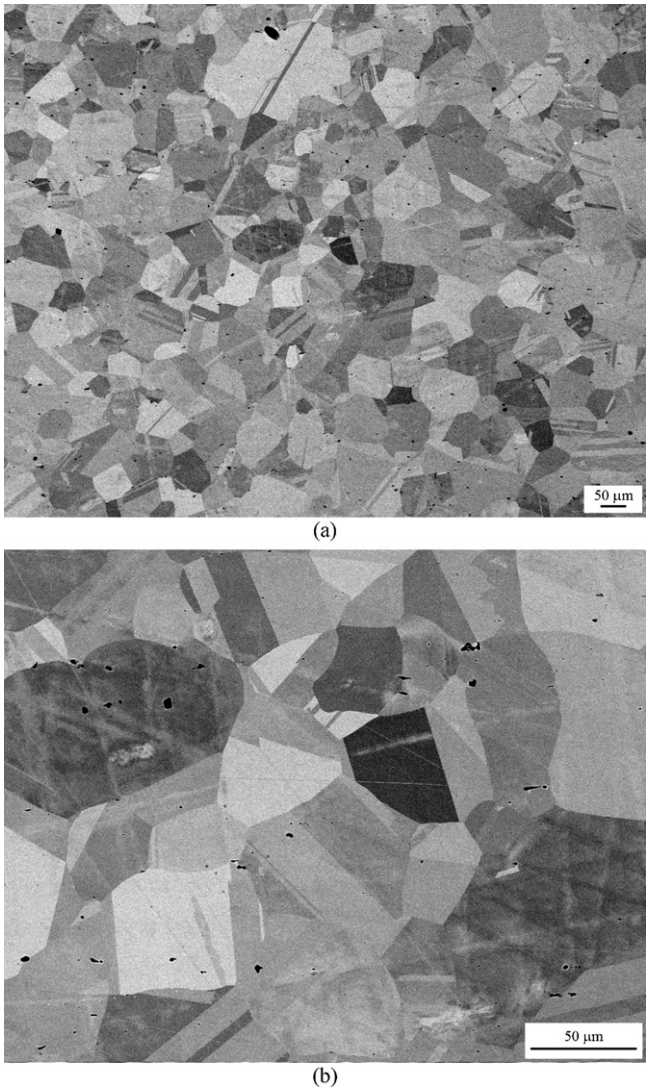

Fig. 2. (a) Low-magnification and (b) high-magnification BSE SEM images of the long section of HAYNES 282 alloy in the baseline condition.

2. Experimental

Commercially available HAYNES 282 alloy sheet was originally provided by HAYNES, International (Kokomo, IN) in the solution-annealed condition, where it can be easily deformed. The typical commercially used solution annealing temperature is in the range of 1394–1422 K (1121–1149 °C). In this study, the commercial sheet was cold rolled to 20% reduction then solution-treated at 1367 K (1094 °C), 1394 K (1121 °C), 1422 K (1149 °C), and 1450 K (1177 °C) for 20 min followed by water quenching (WQ) to evaluate the effect of temperature on the grain size. The intent was to obtain an average grain size well below 100 μm for the creep study. The temperature that provided this was 1367 K (1094 °C) and thereafter this was the chosen temperature for the solution treatments of this alloy. A two-step age hardening treatment is required to put the alloy into the high-strength condition, and this treatment is used to control the γ′ precipitate size and volume fraction. As the intent of this study was to only change the grain boundary structure, an identical age hardening treatment was used on all the samples evaluated. This age-hardening treatment included a treatment of 1283 K (1010 °C) for 2 h followed by cooling to 1061 K

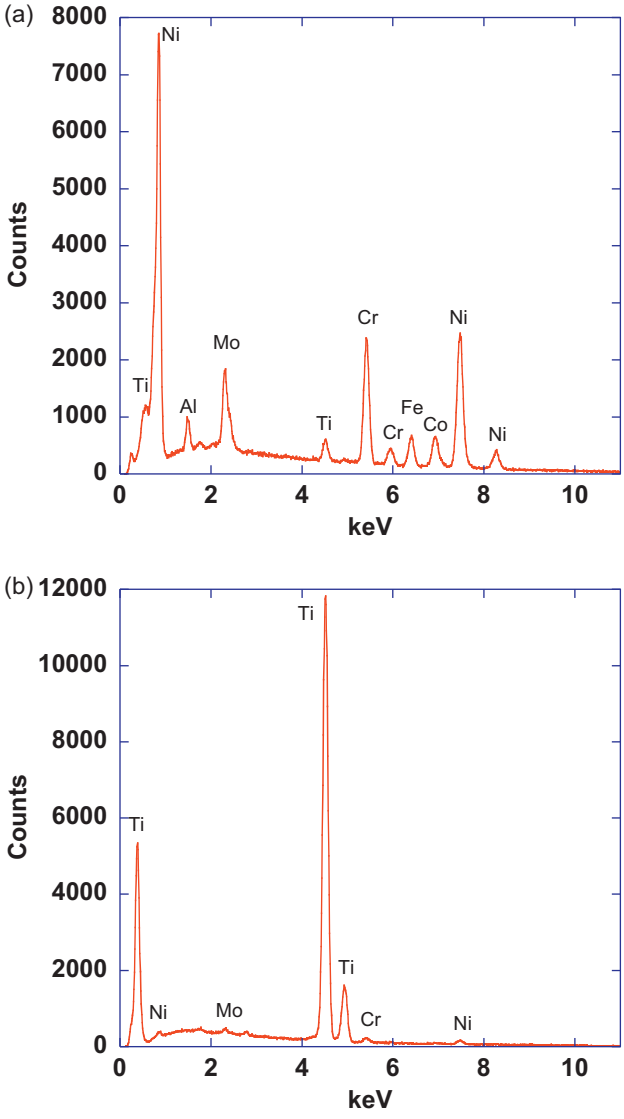

Fig. 3. EDS data of (a) matrix phase and (b) dark precipitate phase in the HAYNES 282 baseline microstructure. The dark precipitates were Ti-rich while the matrix fcc grains were Ni-rich.

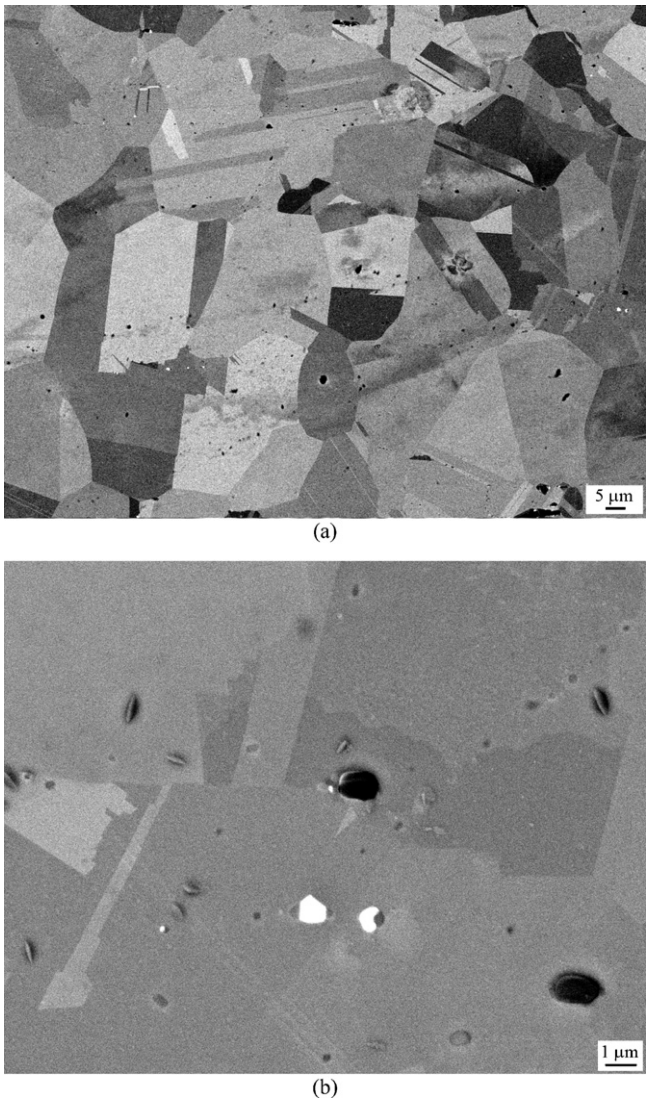

Fig. 4. (a) Low-magnification and (b) high-magnification BSE SEM images of the transverse section of a HAYNES 282 alloy microstructure after the final cold rolling procedure but before the aging treatment.

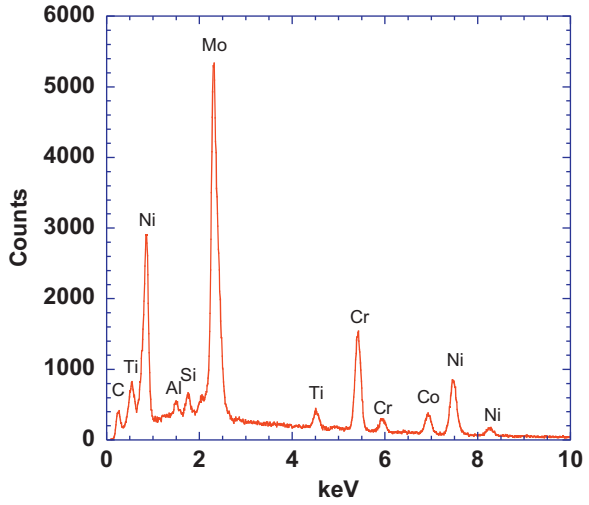

Fig. 5. EDS data of white precipitates in Fig. 4a and b for the HAYNES 282 alloy microstructure after the final cold rolling procedure but before the aging treatment. The white precipitates were Mo-rich while the matrix fcc grains were rich in Ni and Cr.

(788 °C) and holding this temperature for 8 h then cooling to RT. The baseline condition for the HAYNES 282 alloy was the commercially available sheet (solution treated at 1404 K (1131 °C)) that was aged according to the aging treatment just mentioned. Samples in the baseline condition were evaluated in tensile-creep experiments and the data was compared with those for the TMP condition which involved cold rolling the baseline sheet, which was originally approximately 6.4 mm thick, through a sequence of 20% reduction in thickness followed by solution treating at 1367 K (1094 °C) for 20 min. This process was repeated three times and after the final annealing treatment, the sheet, which was now approximately 2.6 mm thick, was cooled to RT and the microstructure was evaluated using electron backscattered diffraction (EBSD) and scanning electron microscopy (SEM). Tensile-creep experiments were performed on this TMP sheet after the above mentioned age-hardening treatment. It is important to note that the solution treatment used for the TMP material was 37 K lower than that used for the baseline material, this resulted in a lower average equiaxed grain size for the TMP material compared with the baseline material.

Commercially available HAYNES 230 alloy was also provided by HAYNES International for a comparison examination. The measured alloy compositions are provided in Table 1. As HAYNES 230 alloy does not require an age-hardening treatment, a simple solution-treatment study, similar to that performed on the HAYNES 282 alloy, was performed to determine the temperature which would result in a reasonably small grain size. Samples were solution treated at 1422 K (1149 °C), 1450 K (1177 °C), 1478 K (1205 °C), and 1505 K (1232 °C) for 20 min followed by WQ. Based on the microstructural observations, a solution treatment temperature of 1422 K (1149 °C) was chosen for the intermediate annealing steps used to process the TMP material for this alloy. The TMP condition included four cold rolling passes, each of 20% reduction in thickness, with an intermediate solution treatment of 1422 K (1149 °C)/20 min/WQ between each pass. Like that for the HAYNES 282 alloy, the baseline and TMP conditions were compared in the creep investigation, and the baseline starting material was originally 6.4 mm thick and the TMP material ended up being approximately 2.6 mm thick. Also like that for the HAYNES 282 alloy, the solution treatment used for the HAYNES 230 alloy TMP material was 37 K lower than that used for the HAYNES 230 alloy baseline material, this resulted in a lower average equiaxed grain size for the TMP material compared with the baseline material.

Each baseline and TMP sheet was sectioned and metallographically polished before spatially resolved EBSD orientation maps were obtained using hardware and software manufactured by EDAX-TSL, Inc. (Mahwah, NJ). The three sheet orientations (face, longitudinal, and transverse), see Fig. 1, were characterized. The specimens were ground mechanically using 15 μm, 6 μm and 1 μm diamond suspension for 20 min, respectively, and then polished using 0.06 μm colloidal silica for more than 30 min. The step size

Table 1
Alloy compositions in weight percent.

Alloy	Ni	B	Cr	Co	Fe	Mn	Si	Mo	C	Al	Ti	W
HAYNES 230 alloy	Bal.	0.004	22.3	0.30	1.5	0.47	0.39	1.3	0.10	0.24	<0.01	13.9
HAYNES 282 alloy	Bal.	0.003	19.7	10.1	0.2	0.03	<0.05	8.4	0.064	1.5	2.1	<0.01

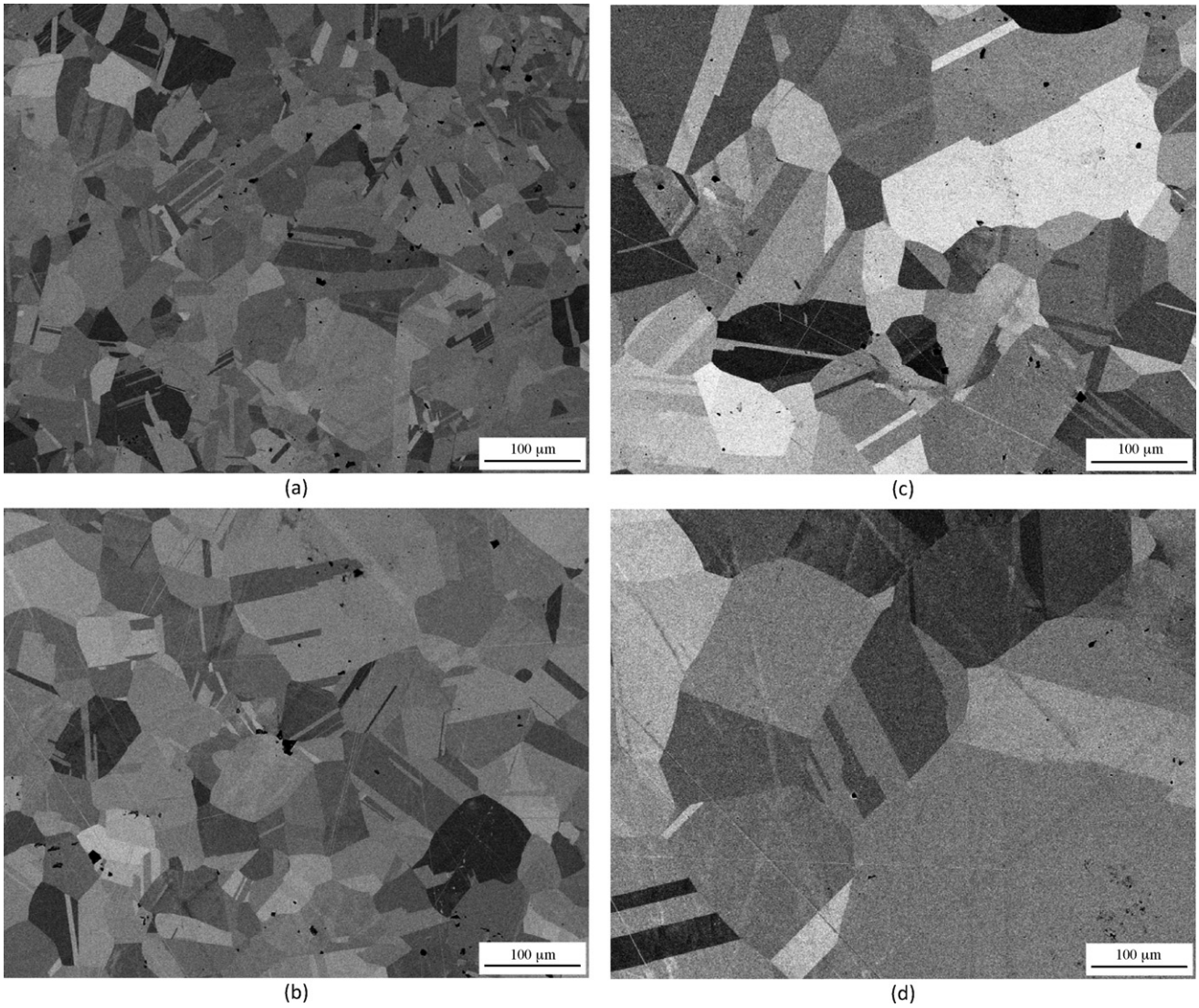

Fig. 6. BSE SEM images of the face section of the HAYNES 282 alloy after the following solution treatment anneals: (a) 1367 K (1094 °C)/20 min/WQ, (b) 1394 K (1121 °C)/20 min/WQ, (c) 1422 K (1149 °C)/20 min/WQ, and (d) 1450 K (1177 °C)/20 min/WQ.

used to obtain the EBSD orientation maps ranged between 2 and 4 μm and over 1000 grains were analyzed per orientation map. Brandon's criterion [21] was used to distinguish between general high angle grain boundaries (GHAB) and coincident site lattice boundaries (CSLB). The GBCD was obtained using the measured fractions of GHAB (having a misorientation greater than 15°), low angle boundaries (LAB: having a misorientation less than 15°), CSLB (the reciprocal of the fraction of coincident atomic sites between two grains at the grain boundary for Σ5 to Σ27, where a boundary with one coincident atom site in every five is denoted Σ5), and twins (Σ3 having 1/3 coincident sites). These measurements were averaged from several orientation maps taken from the three sheet orientations. Data cleanup was performed. Less than 6% of the points were changed for all of the scans. The precipitate volume fractions were determined using ImageJ image analysis software on backscattered electron (BSE) SEM images acquired using a CamScan44FE Field Emission SEM, an FEI XL-30 FEG SEM, a Zeiss EVO LS 25 SEM, and a JEOL 6500F FEG SEM. The later was equipped with a conventional Si(Li) and microcalorimeter energy dispersive spectrometry (EDS) detector, which was used to identify the elements involved in the precipitate phases. The equiaxed grain size of the matrix fcc-phase was determined using the line-intercept method [22].

Tensile-creep specimens, containing a gage width of 12.5 mm and a gage length of approximately 37 mm, were machined from the TMP sheet materials using either electrical discharge machining (EDM) or milling with the tensile axis parallel to the rolling direction. Prior to creep testing, the EDM recast layers were removed through polishing to a finish of approximately 15 μm. Tensile-creep experiments were performed in air using constant-load vertical creep frames manufactured by Applied Test Systems, Inc. (Butler, PA). The creep experiments were performed at temperatures between 973 and 1088 K (700 °C and 815 °C) and stresses between 25 and 225 MPa. Specimen temperatures, which were monitored using two thermocouples strategically placed within the gage section, were kept within 3 K of the target temperature and strain was monitored using a linear variable differential transformer on a 25 mm gage-length high-temperature extensometer. All tests were conducted such that the time to reach the maximum creep load was less than 5 s and the time, load, temperature, and strain were recorded periodically throughout the experiments. During the creep experiments, after the creep strain had proceeded well into the secondary regime, the load was increased or the creep test was discontinued. The tested specimens were cooled under load to minimize recovery of the dislocation substructure. After the experiments were terminated, the

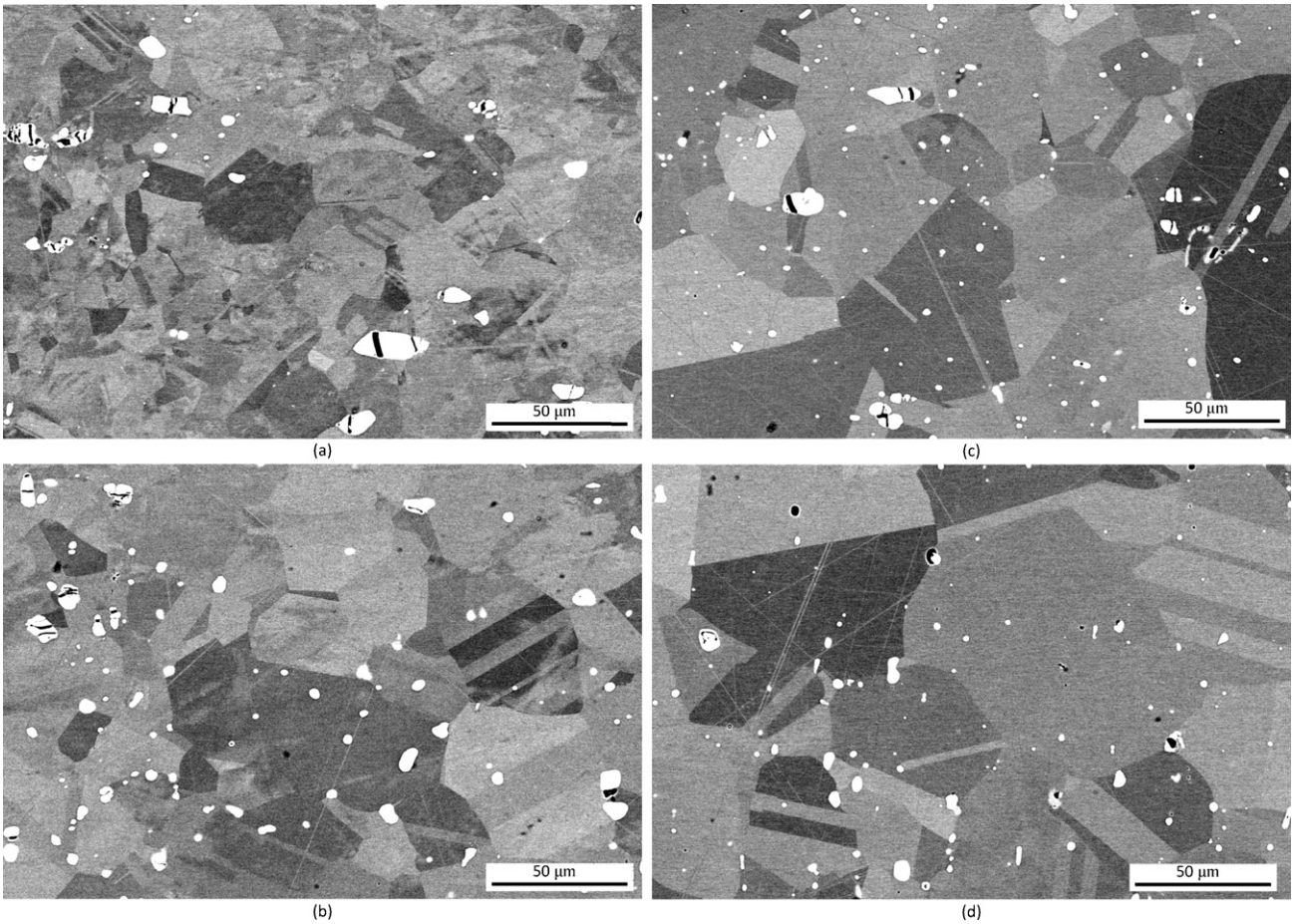

Fig. 7. BSE SEM images of the face section of the HAYNES 230 alloy after the following solution treatment anneals: (a) 1422 K (1149 °C)/20 min/WQ, (b) 1450 K (1177 °C)/20 min/WQ, (c) 1478 K (1205 °C)/20 min/WQ, and (d) 1505 K (1232 °C)/20 min/WQ.

gage sections of the samples were sectioned and examined using SEM.

In addition to the creep experiments open-air, load controlled, tension–tension ($R = 0.1$) fatigue experiments were performed at a temperature of 1088 K (815 °C) using a test frequency of 5 Hz. The maximum applied stress for the fatigue tests was 175 MPa. Strain was monitored using an alumina-rod high-temperature extensometer, with a 12 mm gage length, attached to the gage section of the specimen. The strain-life behavior was documented throughout the experiments. The specimens were locally heated using a Barber Coleman temperature controller and two sets of heating banks, located approximately 5 mm above and below the sample, each containing four evenly spaced quartz lamps. Specimen temperatures were monitored by four chromel–alumel type-K thermocouples located within the specimen's gage section. The targeted test temperature was maintained within ±5 °C. The test specimens were soaked at 1088 K (815 °C) for more than 20 min prior to applying load in order to minimize the thermal stresses. The samples were unloaded after 1 million cycles and prior to fracture, and the deformed gage sections were evaluated using SEM.

3. Results and discussion

3.1. Microstructure

Fig. 2 illustrates a BSE SEM image of HAYNES 282 alloy in the baseline condition. The dark precipitates, which were typically finer than 1 μm, were Ti-rich (see Fig. 3b) and made up 0.34% ± 0.2% of the microstructure. These precipitates were evident after solutionizing followed by quenching as well as after aging. Fig. 4 illustrates the TMP HAYNES 282 alloy microstructure before the final aging treatment. A very small volume of Mo-rich (see Fig. 5) precipitates, bright phase in Fig. 4, was present in this alloy.

Figs. 6a–d and 7a–d illustrate the HAYNES 282 alloy and HAYNES 230 alloy microstructures, respectively, after their solution treatments. The fcc-matrix equiaxed grain size increased with increased solution treatment temperature. The corresponding grain sizes are listed in Table 2. The HAYNES 282 alloy exhibited a significantly larger grain size than the HAYNES 230 alloy for identical solution treatments. The grain size of the alloys in the baseline condition were larger than those in the TMP condition, see Table 3, and this was a result of the higher solution-treatment temperatures used for the commercially available products.

Fig. 8 illustrates BSE SEM images of the HAYNES 230 alloy microstructure after the second cold rolling pass and before the

Table 2
Grain size for the solution treated samples.

Alloy	Solution treatment	Grain size [μm]
HAYNES 282 alloy	1367 K (1094 °C)/20 min/WQ	70
HAYNES 282 alloy	1394 K (1121 °C)/20 min/WQ	95
HAYNES 282 alloy	1422 K (1149 °C)/20 min/WQ	136
HAYNES 282 alloy	1450 K (1177 °C)/20 min/WQ	177
HAYNES 230 alloy	1422 K (1149 °C)/20 min/WQ	35
HAYNES 230 alloy	1450 K (1179 °C)/20 min/WQ	66
HAYNES 230 alloy	1478 K (1205 °C)/20 min/WQ	90
HAYNES 230 alloy	1505 K (1232 °C)/20 min/WQ	121

WQ: water quenched.

Table 3
Grain boundary character distribution of the alloys.

Alloy	Condition	GHAB	LAB	CSLB (Σ3)	LAB + CSLB	Grain size [μm]
HAYNES 282 alloy	Baseline	0.35	0.15	0.50 (0.45)	O.65	106
HAYNES 282 alloy	TMP	0.38	0.03	0.59 (0.50)	0.62	72
HAYNES 230 alloy	Baseline	0.43	0.07	0.51 (0.46)	0.57	57
HAYNES 230 alloy	TMP	0.43	0.04	0.53 (0.46)	0.57	38

solution treatment. The fcc-matrix grain boundaries are significantly deformed while the precipitate boundaries (white phases in Fig. 8) were readily apparent suggesting that the grains deformed more easily than the precipitates. The matrix grains were Ni-rich while the precipitates were W-rich, see Fig. 9. The average volume percent of the precipitates, which ranged up to 15 μm in diameter, was 2.3% ± 0.5%. A previous study of this alloy has shown that the large globular precipitates are M_6C carbides, with M being W, Cr, and Ni, while the smaller precipitates are $M_{23}C_6$ carbides with M being mainly Cr [23]. Both types have a cubic structure [23]. The effect of solution treatment on the cold-rolled microstructure is apparent through comparing Fig. 8 with Fig. 10, which illustrates the TMP HAYNES 230 alloy microstructure.

Table 3 indicates the fraction of the different grain boundary types that were present in each of the alloys. It can be seen that approximately half of boundaries were twins and 35–43% of the grain boundaries were GHABs. The majority of the boundaries were categorized as CSLB + LAB. This is typical when Ni-base superalloys are processed using a strain–recrystallization processing methodology [3–20,24]. However, the TMP material did not exhibit a significantly different GBCD than the baseline material. Thus, although the TMP methodology used, which involved a cyclic treatments involving a significant amount of deformation followed by short recrystallization-annealing treatments, was intended to increase the CSLB + LAB fractions (as it has been used successfully in this endeavor previously [5,6]), the GBCD for these alloys was not significantly changed. Thus, the additional cost involved in using

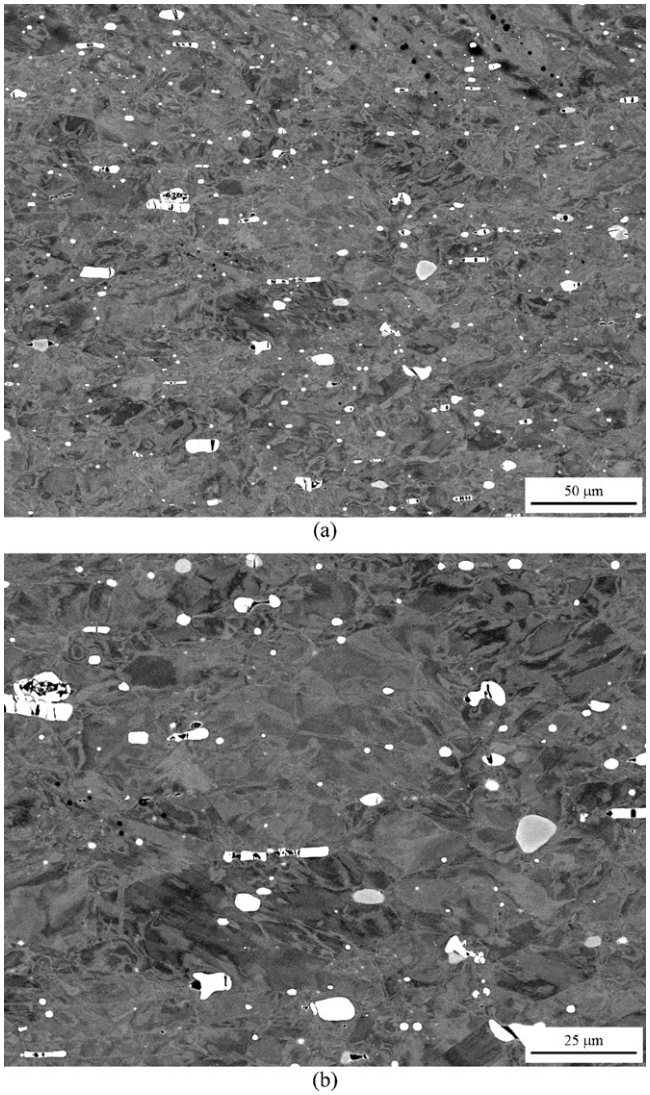

Fig. 8. (a) Low-magnification and (b) high-magnification BSE SEM images of the transverse section of a HAYNES 230 alloy microstructure after the second rolling pass but before the subsequent solution treatment.

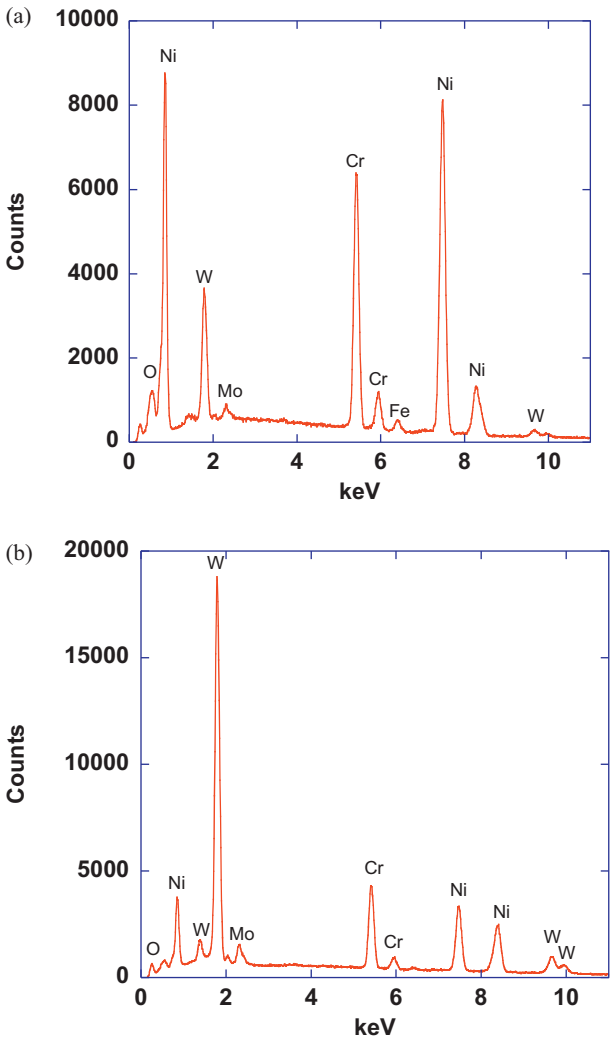

Fig. 9. EDS data taken from the (a) entire area represented in Fig. 8 and from only the (b) white precipitate phase in Fig. 8 for the HAYNES 230 alloy after the second rolling pass but before the subsequent solution treatment. The precipitates were W-rich while the matrix fcc grains were rich in Ni and Cr.

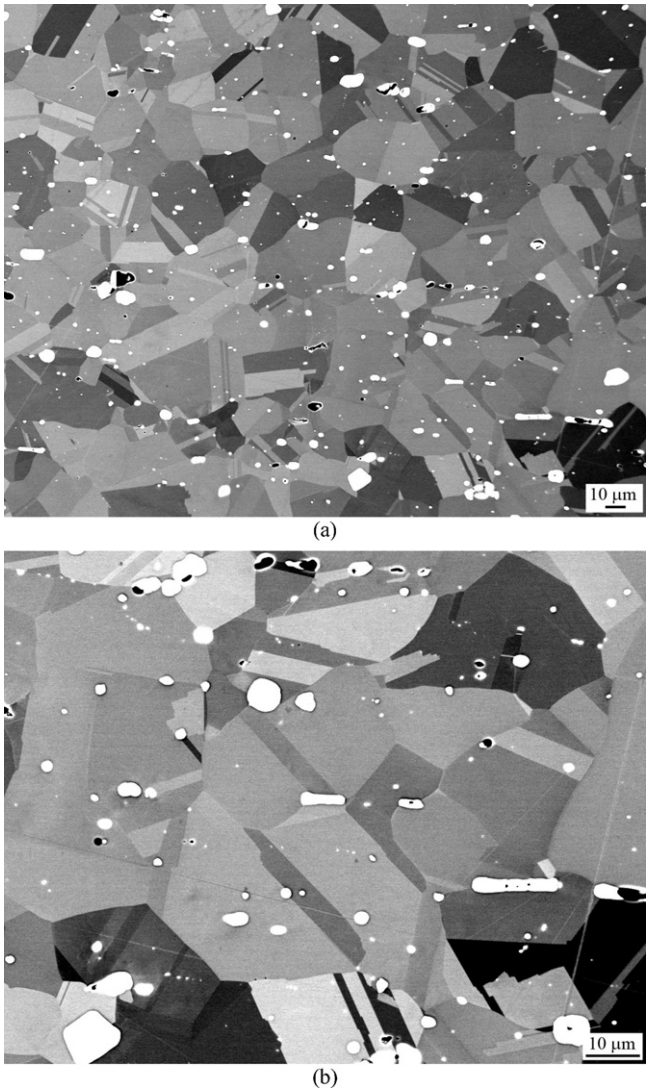

Fig. 10. (a) Low-magnification and (b) high-magnification BSE SEM images of the transverse section of the HAYNES 230 alloy in the TMP condition.

these energy-intensive treatments was not beneficial in significantly changing the GBCD. In fact, they resulted in a finer grain size which can have detrimental effects on the creep resistance. It is possible that an alternatively designed TMP scheme also proposed for grain boundary engineering [5], involving less cold work and longer annealing times, is necessary to impose significant changes in the GBCD for these alloys. Pole figure analysis based on the EBSD data indicated that the alloys were not strongly textured. Thus, the TMP treatments did not introduce a preferred texture in the alloys, and this result has also been observed previously for superalloys processed using an identical processing methodology [19,20,24].

3.2. Creep behavior

For each alloy, the creep strain-life history resembled that for most metals exhibiting three stages of creep: primary, secondary and tertiary [25,26]. Once the creep stress was reached, there was usually a short incubation period before a positive creep strain rate was achieved and in many cases the creep strain decreased after the full load was applied. Fig. 11 illustrates creep strain versus time plots for HAYNES 282 alloy in the baseline and TMP conditions at $T = 1088$ K (815 °C) and $\sigma = 100$ MPa. Fig. 12 illustrates creep strain versus time plots for HAYNES 230 alloy in the baseline and TMP

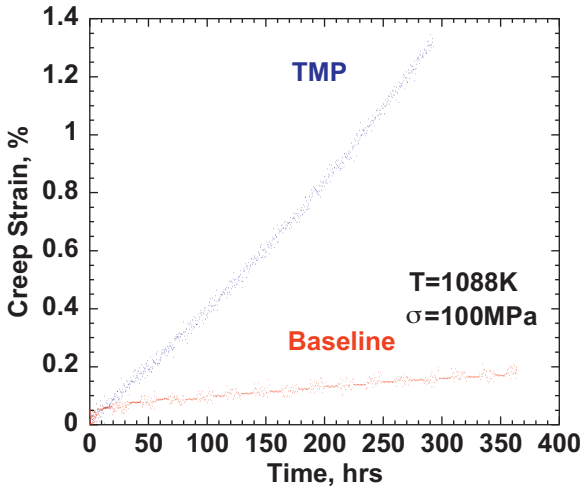

Fig. 11. Creep strain versus time plot ($T = 1088$ K (815 °C) and $\sigma = 100$ MPa) for the HAYNES 282 alloy in the baseline and TMP conditions.

conditions. Each alloy exhibited greater creep rates in the TMP condition compared with the baseline condition. The larger grain sizes of the baseline materials may have contributed to this result. Fig. 13 illustrates creep strain versus time plots for both the HAYNES 230 alloy and HAYNES 282 alloy in the TMP conditions at $T = 1033$ K

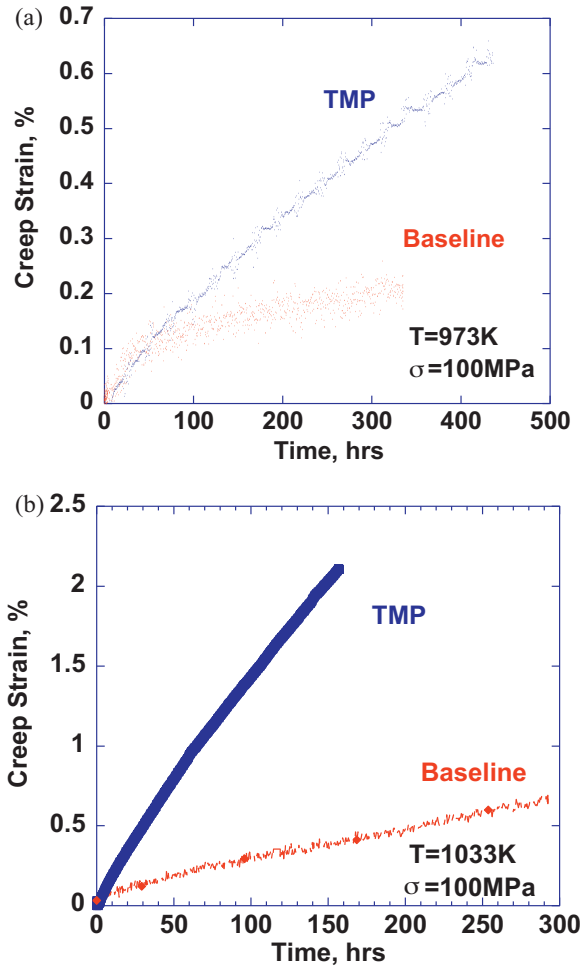

Fig. 12. Creep strain versus time plot (a) $T = 973$ K (700 °C) and $\sigma = 100$ MPa and (b) $T = 1033$ K (760 °C) and $\sigma = 100$ MPa for the HAYNES 230 alloy in the baseline and TMP conditions.

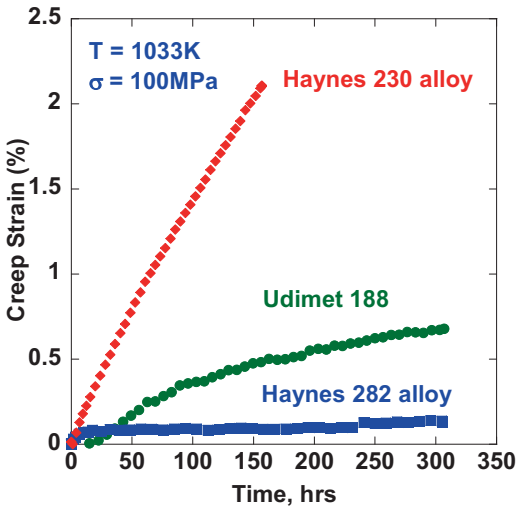

Fig. 13. Creep strain versus time plot (T = 1033 K (760 °C) and σ = 100 MPa) for the HAYNES 230 and 282 alloys in the TMP condition and Udimet 188 [20].

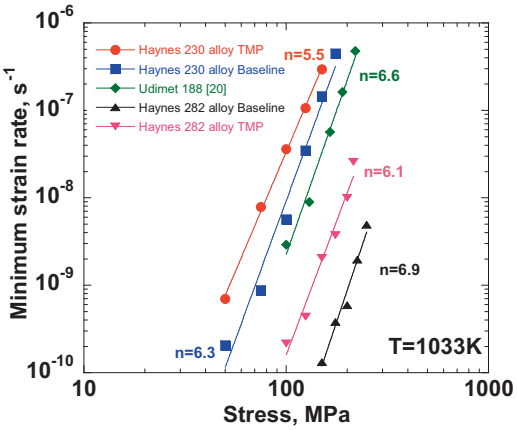

Fig. 15. Log minimum creep strain versus log stress plot for each studied TMP alloy at T = 1033 K (T = 760 °C) and 50 MPa ≤ σ ≤ 225 MPa. These plots were used to calculate the listed stress exponent (n) values. It is evident that HAYNES 282 alloy exhibited significantly lower minimum creep rates than HAYNES 230 alloy. Data for Udimet 188 alloy is also included [20]. The Udimet 188 alloy exhibited creep resistance intermediate to that for the HAYNES alloys 230 and 282.

(760 °C) and σ = 100 MPa. The HAYNES 282 alloy exhibited significantly lower creep strains and strain rates than the HAYNES 230 alloy. As HAYNES 230 alloy was designed for applications at higher temperatures where the γ′-strengthened alloys, such as HAYNES 282 alloy, lose strength due to γ′ solutionizing, the worse creep resistance of HAYNES 230 alloy is not unexpected. Comparison with a Udimet 188 alloy, that was processed using a cold rolling scheme of 35%, 35%, 35%, and 25% [20], shows that the Udimet 188 alloy exhibited better creep resistance than HAYNES 230 alloy yet worse creep resistance than HAYNES 282 alloy, see Fig. 13.

The minimum creep rates were used for calculating the creep stress exponent (n) using the power law creep equation:

$$\text{minimum creep rate} = A\sigma^n \quad \exp\left(\frac{-Q_{app}}{RT}\right) \tag{1}$$

where A is a constant, σ is the applied stress, R is the gas constant, T is the absolute temperature, and Q_{app} is the apparent activation energy. Figs. 14 and 15 illustrate a log minimum strain rate versus log stress plot used to calculate the n-values, which were always between 5.0 and 6.9. Based on creep theory for pure metals [25,27], these n-values suggest that dislocation creep was dominant in the secondary creep regime. Fig. 14 indicates the detrimental affect of the TMP treatment on the minimum creep rates, and Fig. 15 indicates that the HAYNES 282 alloy exhibited over an order of magnitude improvement in the minimum creep rates compared with the HAYNES 230 alloy. In addition, Fig. 15 indicates that the Udimet 188 alloy minimum creep rates were approximately a factor of two lower than those for the HAYNES 230 alloy. Fig. 16 is a natural logarithm of the minimum strain rate versus inverse temperature plot used for calculating the Q_{app} values. The measured Q_{app} values were in the range expected for lattice self diffusion based on values from other Ni-base superalloys [19,20,24,28,29]. Thus, combining the n and Q_{app} values, dislocation creep controlled by lattice self-diffusion is considered to be the secondary-creep stage rate controlling mechanism.

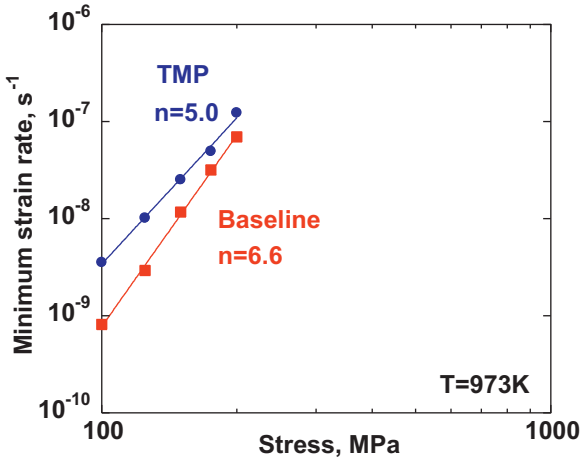

Fig. 14. Log minimum creep strain versus log stress plot for HAYNES 230 alloy in the TMP and baseline conditions at T = 973 K (T = 700 °C) 100 MPa ≤ σ ≤ 200 MPa. These plots were used to calculate the listed stress exponent (n) values.

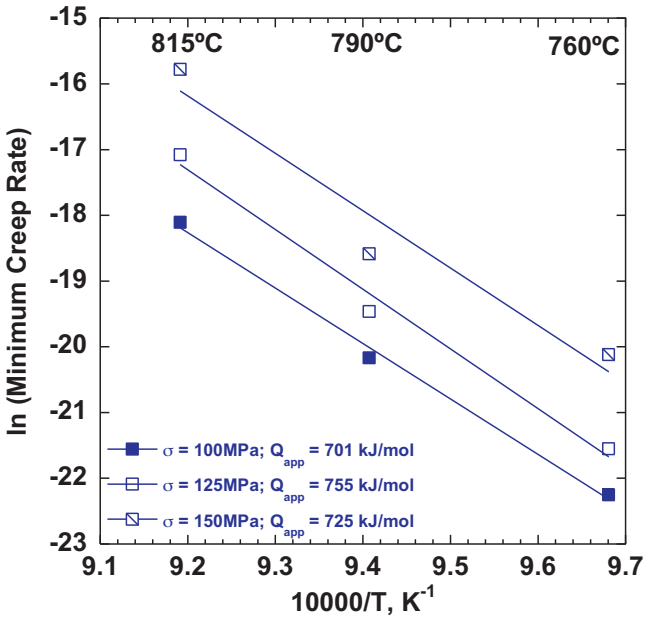

Fig. 16. Ln (minimum creep rate) versus 10,000/T plot used to calculate the Q_{app} values for HAYNES 282 TMP at three different creep stresses.

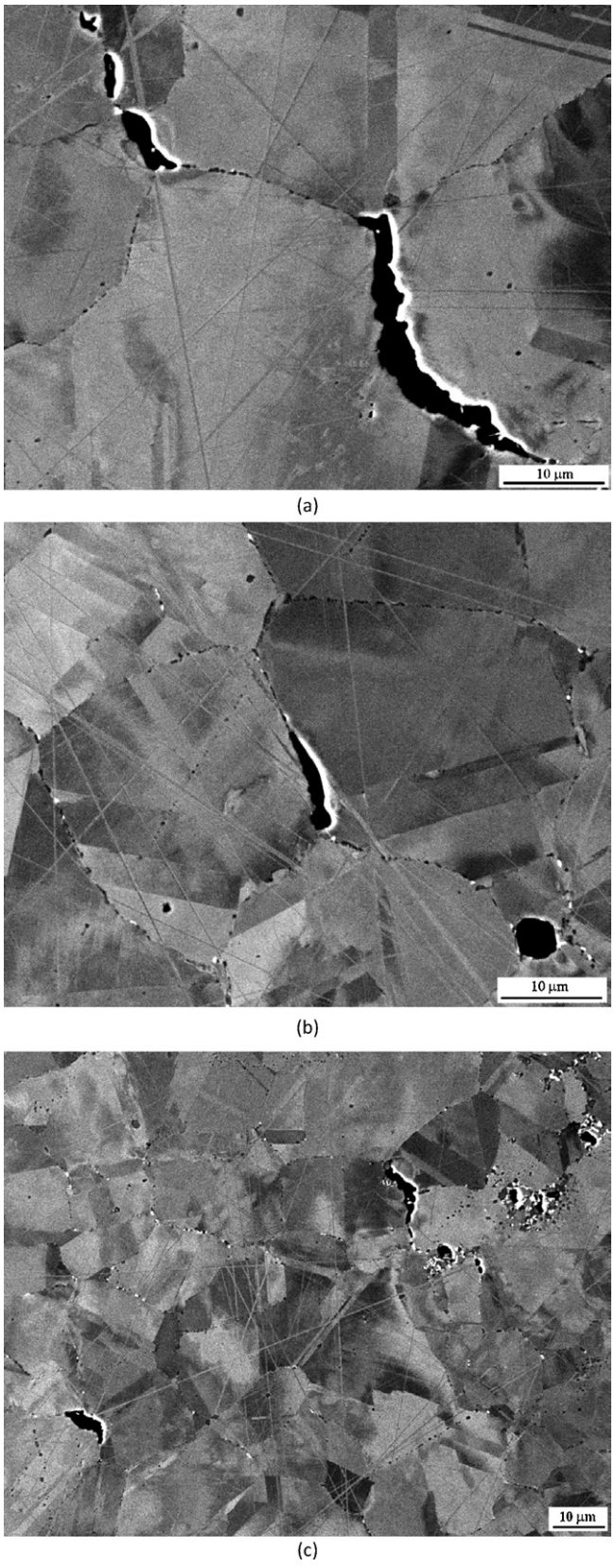

Fig. 17. BSE SEM images of a HAYNES 282 alloy TMP sample which exhibited 7.5% creep strain in 70 h (tertiary regime) after an experiment at $T = 1088$ K (815 °C) and $\sigma = 215$ MPa. This sample exhibited secondary grain boundary cracking.

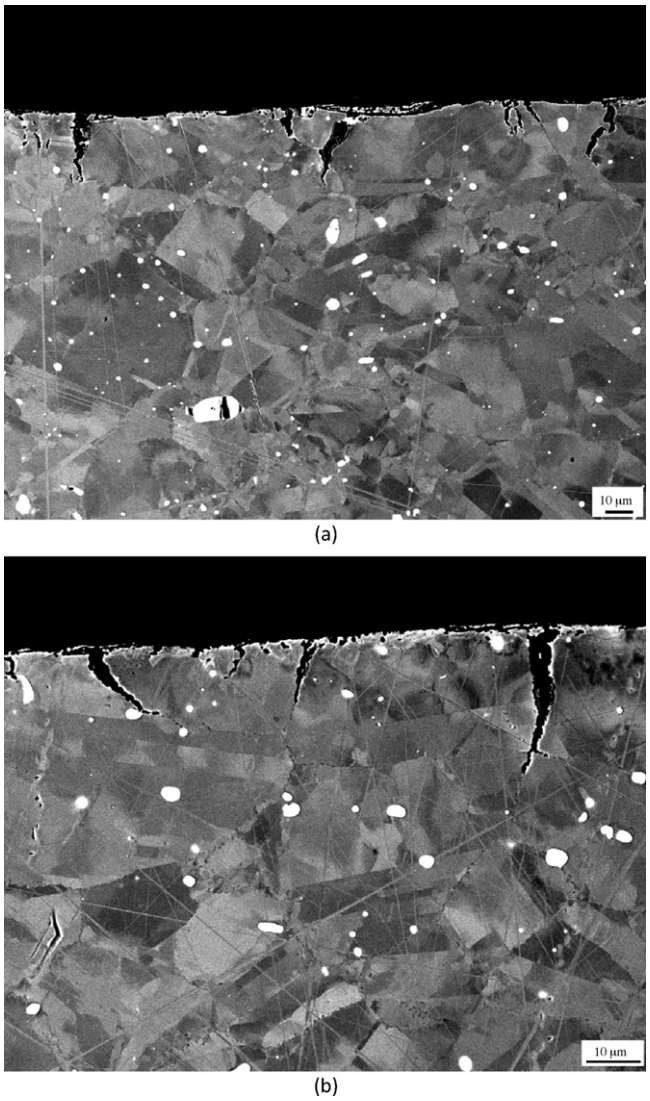

Fig. 18. BSE SEM images of a HAYNES 230 alloy TMP sample which exhibited 10.5% creep strain in 220 h (not tertiary regime) after an experiment at $T = 1033$ K (760 °C) and $\sigma = 100$ MPa with a load jump after 160 h to $\sigma = 150$ MPa. This sample exhibited secondary grain boundary cracking and edge cracking.

Grain boundary cracking was evident in each alloy after creep deformation, see Figs. 17 and 18. However, it is noted that the extent of grain boundary cracking was not as significant as that observed in Udimet 188 [24]. There were no visible flaws or cracks along the grain boundaries after TMP so these cracks developed due to creep deformation. Intergranular cracking has also been observed in HAYNES 230 under creep–fatigue conditions at temperatures ranging between 873 and 1073 K (600 and 800 °C) [30] and in RT tension after being exposed for up to 500 h at 1273 K (1000 °C) [31]. Cracks also tended to form along the sample edges, see Fig. 18. It is noted that the possible fracture of carbide precipitates during the TMP of HAYNES 230 alloy may be an important issue in the development of creep voids in this alloy. An interesting aspect of the deformation behavior of the HAYNES 282 alloy was that the precipitates tended to migrate to the grain boundaries during the elevated-temperature deformation, compare Fig. 17 with Figs. 2, 4 and 6. This migration, also observed in INCONEL 617 [32], was expected to be aided by diffusion and may have also aided the intergranular cracking. Previous work suggested that the redistribution of precipitates occurs by the dissolution, diffusion (along grain boundaries or through grain interiors), and reprecipitation of

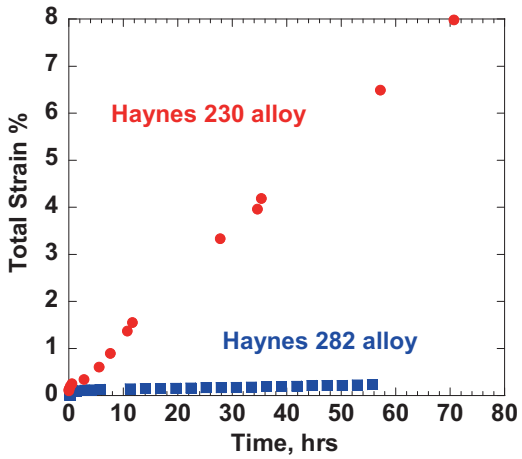

Fig. 19. Total strain versus time plot for a fatigue experiment performed at $T = 1088$ K (815 °C) and $\sigma_{max} = 175$ MPa for the HAYNES 282 and 230 alloys in the TMP condition.

the carbides on the grain boundaries, and it is related to the applied stress [32]. This topic will be the focus of a future work.

Ratcheting (cyclic creep) describes a phenomenon that a material experiences progressive accumulation of deformation under cyclic loading [33]. The total strain versus time plots during the fatigue experiments for each alloy in the TMP condition is plotted in Fig. 19. The total strain was taken at the peak stress of certain cycle numbers and plotted with the elapsed time. These curves closely resemble a typical creep curve exhibiting primary and secondary creep stages. Thus, during the elevated-temperature load controlled fatigue experiment, creep ratcheting was exhibited by these nickel-based superalloys. Similar to the creep behavior, the HAYNES 282 alloy exhibited a much lower total strain and strain rate than the HAYNES 230 alloy, which exhibited a total strain of 8% in 70 h. This behavior can be explained by the superior creep resistance exhibited by the HAYNES 282 alloy. Also similar to the creep behavior, the alloys exhibited some grain boundary cracking, see Fig. 20. This topic will be the focus of a future work.

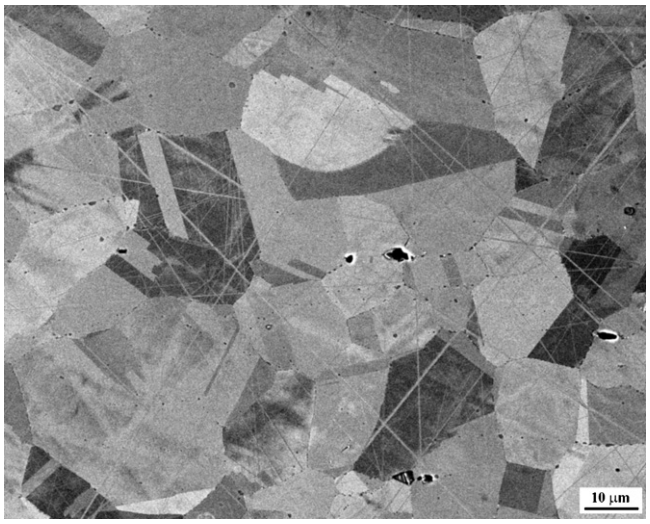

Fig. 20. BSE SEM image of a HAYNES 282 alloy TMP sample which exhibited ~0.3% total strain in 57 h after a fatigue experiment performed at $T = 1088$ K (815 °C) and $\sigma_{max} = 175$ MPa. Some secondary grain boundary cracking was exhibited.

4. Summary and conclusions

This work evaluated the effect of TMP on the microstructure, creep, and fatigue behavior of HAYNES 282 and HAYNES 230 nickel-based superalloys. The TMP treatment did not significantly affect the GBCD. HAYNES 282 alloy was shown to be significantly more creep resistant than HAYNES 230 alloy within the temperature range examined (973–1088 K (700–815 °C)) independent of TMP. The TMP treatment resulted in reduced creep resistance of the alloys. The reduced grain size of the TMP materials, induced by lower solution-treatment temperatures, is considered to have detrimentally affected the creep resistance. For the applied stresses and temperature evaluated, the measured creep exponents suggested that dislocation creep was the dominant creep deformation mechanism independent of the processing condition. The fatigue behavior indicated that creep ratcheting occurred more prominently in the HAYNES 230 alloy than in the HAYNES 282 alloy and this was explained to be a result of the superior creep resistance exhibited by the HAYNES 282 alloy. Thus, this study suggests that additional energy-intensive processing treatments, beyond those involved in the commercially available sheet products, may not be beneficial for additional creep resistance.

Acknowledgements

The authors are grateful to Drs. Lee Pike and Michael Fahrmann of HAYNES International (Kokomo, IN, 46904-9013) for overseeing the alloy processing and for useful comments on the manuscript. The authors acknowledge the assistance of Dr. Yukinori Yamamoto of Oak Ridge National Laboratory (ORNL) for overseeing the heat treatments. A portion of this research was conducted at the SHaRE User Facility, which is sponsored by the Division of Scientific User Facilities, Office of Basic Energy Sciences, U.S. Department of Energy.

References

[1] HAYNES 282 Alloy Bulletin, Kokomo, IN; http://www.haynesintl.com/pdf/h3173.pdf.
[2] HAYNES 230 Alloy Bulletin, Kokomo, IN; http://www.haynesintl.com/pdf/h3000.pdf.
[3] B. Alexandreanu, B.M. Capell, G. Was, Mater. Sci. Eng. A 300 (2001) 94–104.
[4] C. Cheung, U. Erb, G. Palumbo, Mater. Sci. Eng. A 185 (1994) 39–43.
[5] V.R. Dave, M.J. Cola, M. Kumar, A.J. Schwartz, G.N.A. Hussen, Weld. J. (2004) 1-S–5-S.
[6] W.E. King, A.J. Schwartz, Scripta Mater. 38 (1998) 449–455.
[7] U. Krupp, W.M. Kane, X. Liu, X.O. Dueber, C. Laird, C.J. McMahon, Mater. Sci. Eng. A 349 (2003) 213–217.
[8] U. Krupp, W.M. Kane, C. Laird, C.J. McMahon, Mater. Sci. Eng. A 387–389 (2004) 409–413.
[9] E.M. Lehockey, G. Palumbo, Mater. Sci. Eng. A 237 (1997) 168–172.
[10] E.M. Lehockey, G. Palumbo, P. Lin, A.M. Brennenstuhl, Scripta Mater. 36 (1997) 1211–1218.
[11] E.M. Lehockey, G. Palumbo, P. Lin, Metall. Mater. Trans. A 29 (1998) 3069–3079.
[12] P. Lin, G. Palumbo, U. Erb, K.T. Aust, Scripta Mater. 33 (1995) 1387–1392.
[13] G. Palumbo, Metal alloys having improved resistance to intergranular stress corrosion cracking. U.S. Patent 5,817,193 (1998).
[14] G. Palumbo, K.T.K.T. Aust, in: D. Wolf, S. Yip (Eds.), Materials Interfaces: Atomic Level Structure and Properties, 1st ed., Chapman and Hall, New York, 1989, pp. 190–211.
[15] G. Palumbo, K.T. Aust, Acta Metall. Mater. 38 (1990) 2343–2352.
[16] G. Palumbo, E.M. Lehockey, P. Lin, J. Met. 50 (1998) 40–43.
[17] V. Thaveeprungsriporn, G.S. Was, Metall. Mater. Trans. A 28 (1997) 2101–2112.
[18] G.S. Was, V. Thaveeprungsriporn, D.C. Crawford, J. Met. 50 (1998) 44–49.
[19] C.J. Boehlert, D.S. Dickmann, N.C. Eisinger, Metall. Mater. Trans. A 37 (2006) 27–40.
[20] S.C. Longanbach, C.J. Boehlert, in: C.R. Roger, A.G. Kenneth, C. Pierre, G. Timothy, G.F. Michael, S.H. Eric, A.W. Shiela (Eds.), Proceedings of Superalloys 2008 (11th International Symposium on Superalloys), (TMS, Warrendale, PA), 2008, pp. 461–468.
[21] D.G. Brandon, Acta Metall. 14 (1966) 1479–1484.
[22] Standard Test Methods for Determining Average Grain Size, ASTM Designation E112-96e3, ASTM, West Conshohocken, PA.
[23] D. Kim, I. Sah, C. Jang, J. Nucl. Mater. 405 (2010) 9–16.
[24] C.J. Boehlert, S.C. Longanbach, T.R. Bieler, Philos. Mag. 88 (2008) 641–664.

[25] R.W. Evans, B. Wilshire, Creep of Metals and Alloys, 1st ed., The Institute of Metals, New York, 1985, pp. 9–14.
[26] R.W. Hertzberg, Deformation and Fracture Mechanics of Engineering Materials, 4th ed., John Wiley and Sons, New York, 1996.
[27] F.W. Crossman, M.F. Ashby, Acta Metall. 23 (1975) 425.
[28] C.L. Meyers, J.C. Shyne, O.D. Sherby, Aust. Inst. Met. 8 (1963) 171.
[29] B.A. Wilcox, A.H. Clauer, Met. Sci. J. 3 (1969) 26.
[30] A.K. Roy, S. Chatterjee, M.H. Hasan, J. Pal, L. Ma, Mater. Sci. Eng. A 527 (2010) 4830–4836.
[31] D. Kim, I. Sah, C. Jang, J. Nucl. Mat. 405 (2010) 9–16.
[32] S. Schlegel, S. Hopkins, E. Young, J. Cole, T. Lillo, M. Frary, Metall. Mater. Trans. A 40 (2009) 2812–2823.
[33] T. Hassan, S. Kyriakides, Int. J. Plast. 10 (1994) 149–184.